Simultaneous LEO Satellite Tracking and Differential LEO-Aided IMU Navigation

Joe Saroufim, Samer Watchi Hayek, and Zaher M. Kassas
Department of Electrical and Computer Engineering
The Ohio State University
Columbus, OH, USA
saroufim.1@osu.edu, watchihayek.1@osu.edu, zkassas@ieee.org

***Abstract*—A navigation framework with differential measurements from low Earth orbit (LEO) satellite signals of opportunity is presented. This framework comprises a navigating rover with unknown states and one or more base stations with known position(s). The framework fuses differenced pseudorange or Doppler measurements from the rover and base station(s) to LEO satellites with *unkown* states, in an extended Kalman filter (EKF)-based tightly-coupled LEO-aided inertial navigation system (INS), while estimating the rover's states simultaneously with the LEO satellites' states. Simulations are conducted to analyze the navigation performance due to including a varying number of differential base stations. The simulations considered an aerial vehicle equipped with a tactical-grade inertial measurement unit (IMU), an altimeter, a GNSS receiver, and a LEO receiver making pseudorange and Doppler measurements to 14 Starlink LEO satellites. The vehicle-mounted receiver clock was assumed to be an oven-controlled crystal oscillator (OCXO), while the satellites were equipped with chip-scale atomic clocks (CSACs). The aerial vehicle navigated for 28 km in 300 seconds, the last 23 km of which are without GNSS. It is shown that despite relying on two-line element (TLE) files for the LEO ephemerides, which suffer from errors on the order of kilometers, the differential framework could achieve submeter-level accuracy when using pseudorange measurements. With 3 bases, the vehicle's three-dimensional (3-D) position root mean-squared error (RMSE) drops dramatically, reaching a position RMSE of 28 cm when using pseudorange measurements and 1.94 m when using Doppler. Experimental results are presented for an unmanned aerial vehicle (UAV) navigating for 2.28 km in 120 seconds, while utilizing differential carrier phase measurements from 2 Orbcomm LEO satellites. It is shown that using TLE+SGP4 for the LEO satellites' ephemerides yields a 3-D position RMSE of 419 m, while the differential framework reduces it to 12.79 m.**

***Index Terms*—LEO, differential navigation, INS, signals of opportunity.**

I. Introduction

Resilient and accurate positioning, navigation, and timing (PNT) are key to ensure safe integration of semi-autonomous and fully-autonomous vehicles into our road networks and national airspace [1]. Conventional vehicular navigation systems fuse measurements from global navigation satellite system (GNSS) receivers with inertial measurement units (IMUs) to take advantage of the complementary attributes of each: the long-term stability of the GNSS navigation solution and the short-term accuracy of the IMU [2]. However, relying on GNSS signals as the sole source for IMU aiding poses an alarming threat: GNSS signals can become unreliable or unavailable due to (i) signal blockage and multipath in deep urban canyons [3], [4], (ii) unintentional interference [5], or (iii) intentional jamming or spoofing [6], [7]. Losing GNSS signals for prolonged periods will result in the accumulation of IMU errors, which compromises the vehicle's operational safety and efficiency.

Signals of opportunity (SOPs) [8], which are ambient radio signals that are not intended for PNT, have been extensively studied over the past decade. SOPs could emanate from terrestrial transmitters, e.g., AM/FM [9], [10], cellular [11], [12], and digital television [13], [14], or extraterrestrial transmitters, e.g., low Earth orbit (LEO) [15]–[20] and geostationary Earth orbit (GEO) satellites [21]. Among terrestrial SOPs, the most accurate navigation solution has been demonstrated with cellular signals, yielding meter-level navigation on ground vehicles [22] and submeter-accurate navigation on unmanned aerial vehicles (UAVs) [23]. In recent years, LEO space vehicles (SV) signals have gained significant attention as an attractive PNT source to provide a navigation solution in a standalone fashion [24]–[29] or as an IMU aiding source [30], [31].

LEO SVs possess attractive attributes for PNT [32]. First, the number of LEO SVs engulfing the Earth is rapidly growing, with private tech giants, such as Amazon, SpaceX, and OneWeb planning to launch tens of thousands of LEO SVs into space. The sheer number of SVs and their orbital diversity offers favorable geometric dilution of precision, which yields precise position and velocity estimates. Second, LEO SVs are located about twenty times closer to Earth compared to GNSS which reside in MEO, making LEO SVs' received carrier-to-noise ratio up to 30 dB higher than GNSS. Third, the higher travel speeds of LEO SVs present an advantage over their GNSS counterparts, as rapid dynamics lead to informative Doppler measurements. Fourth, the presence of various LEO megaconstellations transmitting in a wide swath of the spectrum improves robustness against unintentional interference and intentional jamming and spoofing.

Multiple challenges need to be addressed to enable the exploitation of LEO SV signals for PNT in an opportunistic fashion. First, megaconstellation LEO SV operators do not

This work was supported in part by the the Air Force Office of Scientific Research (AFOSR) under Grant FA9550-22-1-0476, in part by the Office of Naval Research (ONR) under Grant N00014-19-1-2511, in part by the National Science Foundation (NSF) under Grant 2240512, and in part by the Aerospace Corporation under Award 4400000428.

necessarily disclose much information about their proprietary signals. To address this challenge, the recently established paradigm of cognitive opportunistic navigation [33], which estimates the minimally known LEO SV signals in a blind fashion has been showing tremendous promise [34]. Most recently, this paradigm allowed for the exploitation of the unknown Starlink [35] and OneWeb [36] LEO SVs, from which navigation observables were produced.

Second, unlike GNSS SVs that periodically transmit their ephemeris in the navigation message, LEO SVs do not publicly transmit information about their position, velocity, and time. The orbital elements of an SV are published and updated daily by the North American Aerospace Defense Command (NORAD) in the format of two-line element files (TLE); where the first line consists of designation and temporal data, while the second line lists the SV Keplerian elements: inclination, right ascension of ascending node, eccentricity, argument of perigee, mean anomaly, and mean motion [37]. TLE data can be used to initialize orbit determination algorithms, such as simplified general perturbation 4 (SGP4) [38], to estimate the SV's position and velocity. However, orbit propagation accumulates position errors on the order of a few kilometers, which will in turn induce errors in the navigation solution. To address this challenge, the simultaneous tracking and navigation (STAN) framework has been proposed, in which the vehicle-mounted receiver estimates its own states simultaneously with the states of the LEO SVs, while aiding the vehicle-mounted IMU with LEO SV observables [39].

Third, the clock states of a LEO SV are unknown, as opposed to GNSS SVs that transmit their clock errors to users through the navigation message. Moreover, one cannot expect LEO SVs to be equipped with highly stable oscillators, such as the ones onboard GNSS SVs, nor to be as tightly synchronized. To address the second challenge, an approach to adaptively estimate LEO satellites' clock stability has been recently developed [40], while [41] proposed a model that considered the systematic effects related to the environment and relativistic effects to improve LEO clock prediction.

Differential positioning is a multiple-receiver PNT technique that entails computing corrections at a known base station to improve the positioning solution at an unknown rover [42], [43]. When the base and the rover are sufficiently close to each other, differential positioning significantly reduces the effect of common mode errors (e.g., SV ephemeris, SV clock errors, and ionospheric and tropospheric errors). Differential positioning with GNSS signals has been thoroughly studied during the past decades yielding centimeter-level accuracy [44]. In the context of LEO-based navigation, differential positioning has been demonstrated using carrier phase measurements from Orbcomm SVs [45] and Doppler measurements from Starlink [46] and Iridium [47].

This paper presents the first study revealing the tremendous potential of employing differential measurements to significantly reduce LEO satellite errors within the STAN framework. This paper makes the following contributions. First, a differential STAN framework is presented, where a single difference measurement model is integrated into the STAN framework to compensate for common mode errors, namely LEO SV ephemerides, LEO SV clocks, and atmospheric delays. The estimation of the navigating vehicle's states and the tracking of the LEO SVs' states is performed in an extended Kalman filter (EKF)-based tightly-coupled LEO-aided inertial navigation system (INS) with two types of LEO observables: pseudorange and Doppler. Next, extensive simulation results from a high-fidelity simulator are presented demonstrating the efficacy of the proposed differential STAN framework. The simulation environment considered an aerial vehicle equipped with a tactical-grade IMU, an altimeter, a GNSS receiver, and a LEO receiver making pseudorange and Doppler measurements to 14 Starlink LEO SVs. The vehicle-mounted receiver was assumed to be an oven-controlled crystal oscillator (OCXO), while the SVs were equipped with chip-scale atomic clocks (CSACs). The aerial vehicle navigated for 28 km in 300 seconds, the last 23 km of which in 240 seconds were without GNSS. It is shown that while pseudorange measurements yield low estimation errors in the differential STAN framework, Doppler measurements are still effective. The effect of including differential base stations on the navigation solution are also studied, showing that remarkably, the inclusion of only a single base results in submeter accuracy when using pseudorange measurements, despite relying on TLE files for the LEO ephemerides, which suffer from errors on the order of kilometers. With 3 bases, the vehicle's position three-dimensional (3-D) root mean-squared error (RMSE) drops dramatically, reaching 28 cm when using pseudorange measurements and 1.94 m when using Doppler. Finally, experimental results are presented for a UAV navigating for 2.28 km in 120 seconds, while utilizing differential carrier phase measurements from 2 Orbcomm LEO SVs. It is shown that using TLE+SGP4 for the LEO SVs' ephmerides yields a 3-D position RMSE of 419 m, while the differential STAN reduces it to 12.79 m.

The rest of the paper is organized as follows. Section II describes the STAN with differential measurements framework. Section III discusses the setup and results of a simulation study that showcases the performance of the proposed framework. Section IV shows experimental results validating the potential of differential STAN. Section V gives concluding remarks.

II. Simultaneous Tracking and Navigation with Differential Measurements

This section formulates the differential STAN framework, summarized in Fig. 1. The framework assumes an environment comprising a mobile rover with unknown states and N stationary base stations with known position(s). The rover and base stations make pseudorange or Doppler measurements to L LEO SVs. Each base station sends to the rover a data packet containing the base's position and measurements.

The STAN framework, depicted in the left dotted box in Fig. 2, employs an INS that couples IMU measurements with GNSS and LEO receiver measurements via an EKF in a

tightly-coupled fashion. The differential STAN framework incorporates measurement(s) to the same LEO SVs from known base station(s), depicted in the right dotted box in Fig. 2.

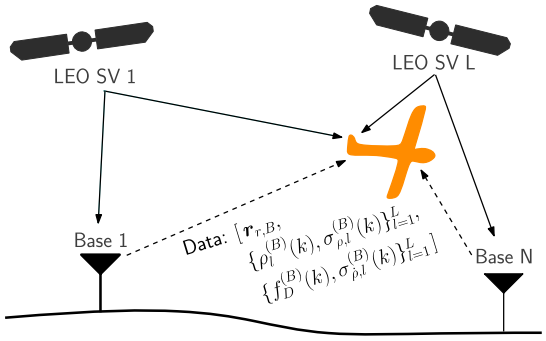

Fig. 1. Differential STAN framework: N base stations with known positions and a rover (UAV) with unknown states make pseudorange or Doppler measurements to the same L LEO SVs. The base stations transmit a data packet containing the base's position $\boldsymbol{r}_{r,B}$ and its pseudorange $\rho_l^{(B)}(k)$ or Doppler $f_D^{(B)}(k)$ measurements to all LEO SVs along with the measurements' standard deviation $\sigma_{\rho,l}^{(B)}(k)$ and $\sigma_{\dot{\rho},l}^{(B)}(k)$, respectively. The rover aids its onboard IMU with the differential measurements and navigates while estimating its own states simultaneously with the LEO SVs' states.

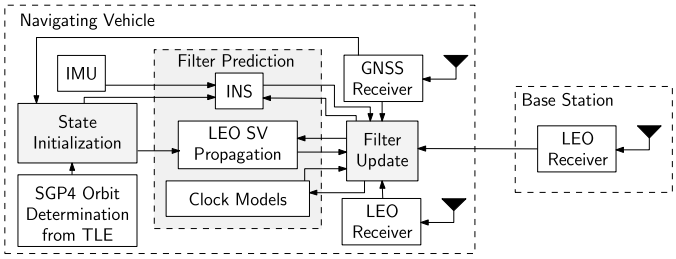

Fig. 2. LEO-aided INS differential STAN framework

A. IMU Model

The IMU measurements are corrupted by noise and sensor bias and are resolved in the vehicle's body reference frame. The IMU consists of a 3-D gyroscope and a 3-D accelerometer that produce angular velocity $\boldsymbol{\omega}_{imu}$ and specific force $\boldsymbol{a}_{imu}$ measurements, respectively, which are modeled as

$$\begin{aligned}\boldsymbol{\omega}_{imu}(k) &= {}^{b}\boldsymbol{\omega}_g(k) + \boldsymbol{b}_{gyr}(k) + \boldsymbol{n}_{gyr}(k)\\ \boldsymbol{a}_{imu}(k) &= \mathbf{R}_g^b(k)[{}^{g}\boldsymbol{a}_b(k) - {}^{g}\boldsymbol{g}(k)] + \boldsymbol{b}_{acc}(k) + \boldsymbol{n}_{acc}(k),\end{aligned}$$

where ${}^{b}\boldsymbol{\omega}_g$ is the true 3-D angular velocity of a coordinate frame $\{b\}$ fixed to the body of the IMU with respect to the global frame$\{g\}$, $\mathbf{R}_g^b$ is a rotation matrix from frame $\{g\}$ to $\{b\}$; ${}^{g}\boldsymbol{a}_b$ is the true 3-D acceleration of $\{b\}$ expressed in $\{g\}$; $\boldsymbol{b}_{gyr}$ and $\boldsymbol{b}_{acc}$ are the gyroscope and accelerometer 3-D biases, respectively; and $\boldsymbol{n}_{gyr}$ and $\boldsymbol{n}_{acc}$ are 3-D measurement noise vectors, which are modeled as white noise sequences with covariances $\mathbf{Q}_{n_{gyr}}$ and $\mathbf{Q}_{n_{acc}}$, respectively.

The gyroscope and accelerometer biases are modeled to evolve according to velocity random walk dynamics as

$$\begin{aligned}\boldsymbol{b}_{gyr}(k+1) &= \boldsymbol{b}_{gyr}(k) + \boldsymbol{w}_{b_{gyr}}(k)\\ \boldsymbol{b}_{acc}(k+1) &= \boldsymbol{b}_{acc}(k) + \boldsymbol{w}_{b_{acc}}(k),\end{aligned}$$

where $\boldsymbol{w}_{b_{gyr}}$ and $\boldsymbol{w}_{b_{acc}}$ are bias instability process noise 3-D vectors, which are modeled as white noise sequences with covariances $\mathbf{Q}_{b_{gyr}}$ and $\mathbf{Q}_{b_{acc}}$, respectively.

B. LEO SV Dynamics Model

SV dynamics can be estimated by employing different orbital propagators, such as SGP4 [38], two-body, and two-body with $J2$ [48]. Although TLE files are frequently updated, they always suffer from an initial error, which accumulates with time, depending on the adopted propagation model. Previous research has shown that open-loop SGP4 propagation may result in localization errors on the order of a few kilometers [49]; hence, they becomes unsuitable for precise STAN solutions. On the other hand, the two-body with $J2$model was found to achieve more reliable and accurate tracking and navigation than the two-body without $J2$model [48]. The latter can propagate the motion of every LEO SV which is defined by the instantaneous Earth's gravitational acceleration a_{grav} and modeled by

$$\ddot{\boldsymbol{r}}_{leo_l}(t) = \boldsymbol{a}_{grav_l}(t) + \tilde{\boldsymbol{w}}_{leo_l}(t), \qquad \boldsymbol{a}_{grav_l}(t) = \frac{\partial U_l(t)}{\partial \boldsymbol{r}_{leo_l}(t)}, \tag{1}$$

where $\boldsymbol{r}_{leo_l} \triangleq [x_{leo_l}, y_{leo_l}, z_{leo_l}]^{\mathsf{T}}$ is the 3-D position vector of the l^{th} LEO SV in the Earth-centered inertial (ECI) frame, U_l is the non-uniform gravitational potential (geopotential) at the SV, and $\tilde{\boldsymbol{w}}_{leo_l}$ is the process noise vector with power spectral density (PSD) $\tilde{\mathbf{Q}}_{leo_l}$ capturing other unmodeled accelerations (e.g, atmospheric drag, solar radiation, general relativity, etc.). The gravitational potential term may be defined by the Joint Gravity Model 3 (JGM-3) developed by the Goddard Space Flight Center [50] where the tesseral and sectoral terms are negligible relative to the zonal terms J_n, and hence may be neglected. This gives

$$U_l(t) = \frac{\mu}{\|\boldsymbol{r}_{leo_l}(t)\|}\left[\sum_{n=2}^{N} J_n \frac{R_E^n}{\|\boldsymbol{r}_{leo_l}(t)\|^2} P_n[\sin(\theta_l)]\right] \tag{2}$$

where μ is the Earth's standard gravitational parameter, P_n is a Legendre polynomial with harmonic n, $\sin(\theta_l) = z_{leo_l}/\|\boldsymbol{r}_{leo_l}\|$, and J_n is the n^{th} zonal coefficient. Knowing that Earth's oblateness is dominated by the J_2 coefficient, the SVs' motion may be derived by combining (1) and (2) as

$$\begin{aligned}\ddot{x}_{leo_l} &= -\frac{\mu x_{leo_l}}{||\boldsymbol{r}_{leo_l}||^3}\left[1 + J_2\frac{3}{2}\left(\frac{R_E}{||\boldsymbol{r}_{leo_l}||}\right)^2\left(1 - 5\frac{z_{leo_l}^2}{||\boldsymbol{r}_{leo_l}||^2}\right)\right]\\ \ddot{y}_{leo_l} &= -\frac{\mu y_{leo_l}}{||\boldsymbol{r}_{leo_l}||^3}\left[1 + J_2\frac{3}{2}\left(\frac{R_E}{||\boldsymbol{r}_{leo_l}||}\right)^2\left(1 - 5\frac{z_{leo_l}^2}{||\boldsymbol{r}_{leo_l}||^2}\right)\right]\\ \ddot{z}_{leo_l} &= -\frac{\mu z_{leo_l}}{||\boldsymbol{r}_{leo_l}||^3}\left[1 + J_2\frac{3}{2}\left(\frac{R_E}{||\boldsymbol{r}_{leo_l}||}\right)^2\left(3 - 5\frac{z_{leo_l}^2}{||\boldsymbol{r}_{leo_l}||^2}\right)\right]\end{aligned} \tag{3}$$

C. Clock Dynamics Model

The dynamics of the clock error states for standalone STAN is assumed to evolve according to the standard double integrator model, driven by process noise [51]. The clock states

for differential STAN follow the same dynamics, evolving as the difference between the receiver's and bases' clock biases and drifts as

$$\boldsymbol{x}_{clk}^{(R,B_n)}(k+1) = \mathbf{F}_{clk}^{(R,B_n)}\boldsymbol{x}_{clk}^{(R,B_n)}(k) + \boldsymbol{w}_{clk}(k), \quad (4)$$

$$\boldsymbol{x}_{clk} \triangleq c \cdot \left[\delta t^{(R,B_1)}, \dot{\delta} t^{(R,B_1)}, ..., \delta t^{(R,B_N)}, \dot{\delta} t^{(R,B_N)}\right]^{\mathsf{T}}$$

$$\delta t^{(R,B_n)} \triangleq \left[\delta t^{(R)} - \delta t^{(B_n)}\right], \quad \dot{\delta} t^{(R,B_n)} \triangleq \left[\dot{\delta} t^{(R)} - \dot{\delta} t^{(B_n)}\right]$$

$$\mathbf{F}_{clk} = \boldsymbol{I}_{N\times N} \otimes \boldsymbol{F}_{clk}^{(R,B_n)}, \qquad \mathbf{F}_{clk}^{(R,B_n)} = \begin{bmatrix} 1 & T \\ 0 & 1 \end{bmatrix}$$

where T is the sampling interval and $\boldsymbol{w}_{clk}$ is the process noise, which is modeled as white noise sequence with covariance $\mathbf{Q}_{clk}$ given by

$$\mathbf{Q}_{clk} = \mathbf{1}_{N\times N} \otimes {\mathbf{Q}_{clk}}^{(R)} + \mathbf{I}_{N\times N} \otimes {\mathbf{Q}_{clk}}^{(B_n)} \quad (5)$$

$$\mathbf{Q}_{clk}^{(i)} = c^2. \begin{bmatrix} S_{\tilde{\omega}_{\delta t,i}} T + S_{\tilde{\omega}_{\dot{\delta} t,i}} \frac{T^3}{2} & S_{\tilde{\omega}_{\dot{\delta} t,i}} \frac{T^2}{2} \\ S_{\tilde{\omega}_{\dot{\delta} t,i}} \frac{T^2}{2} & S_{\tilde{\omega}_{\dot{\delta} t,i}} T \end{bmatrix} \quad (6)$$

where i denotes a base B_n or the rover R, $\otimes$ denotes the Kronecker product, $\mathbf{1}_{N\times N}$ is an $N \times N$ matrix with entries equal to 1, $\mathbf{I}_{N\times N}$ is an $N \times N$ identity matrix, and $S_{\tilde{\omega}_{\delta t,i}}$ and $S_{\tilde{\omega}_{\dot{\delta} t,i}}$ are the clock bias and drift process noise PSDs of the i-th receiver, respectively. These power spectra $S_{\tilde{\omega}_{\delta t_{\dot{\delta}},i}}$ and $S_{\tilde{\omega}_{\dot{\delta} t,i}}$ can be related to the power-law coefficients $\{h_\alpha\}_{\alpha=-2}^{2}$, which have been shown through laboratory experiments to be adequate to characterize the power spectral density of the fractional frequency deviation $y(t)$ of an oscillator from nominal frequency, which takes the form $S_y(f) = \sum_{\alpha=-2}^{2} h_\alpha f^\alpha$ [52]. It is common to approximate the clock error dynamics by considering only the frequency random walk coefficient h_{-2} and the white frequency coefficient h_0, which lead to $S_{\tilde{\omega}_{\delta t,i}} \approx \frac{h_0}{2}$ and $S_{\tilde{\omega}_{\dot{\delta} t,i}} \approx 2\pi^2 h_{-2}$ [51].

D. Measurement Model

In this paper, it is assumed that pseudorange and Doppler measurements from LEO SV signals are available from a specialized receiver. Since LEO SV orbits are above the ionosphere, their signals are subjected to ionospheric and tropospheric delays.

1) Pseudorange Measurement Model: The pseudorange measurement ρ from the i-th receiver to the l-th LEO SV at the k-th time-step is modeled as

$$\begin{aligned} \rho_l^{(i)}(k) &= \|\boldsymbol{r}_{r,i}(k) - \boldsymbol{r}_{leo,l}(k)\|_2 + c \cdot [\delta t_{r,i}(k) - \delta t_{leo,l}(k)] \\ &\quad + c\delta t_{trop,l}^{(i)}(k) + c\delta t_{iono,l}^{(i)}(k) + \nu_{\rho,l}^{(i)}(k), \end{aligned}$$

where $\boldsymbol{r}_{r,i}$ and $\boldsymbol{r}_{leo,l}$ are the 3-D position vectors of the i-th receiver and the l-th LEO SV in the Earth Centered Earth Fixed (ECEF) reference frame; c is the speed of light; $\delta t_{r,i}$ and $\delta t_{leo,l}$ are the clock biases of the i-th receiver and the l-th LEO SV, respectively; $\delta t_{iono,l}^{(i)}(k)$ and $\delta t_{trop,l}^{(i)}(k)$ are the ionospheric and tropospheric delays from the l-th LEO SV to the i-th receiver at time-step k, respectively; and $\nu_{\rho,l}^{(i)}$ is the pseudorange measurement noise, which is modeled as a discrete-time zero-mean white Gaussian sequence with variance $\sigma_{\rho,l}^{(i)}$(k).

The differential pseudorange measurement model across the rover and the base is defined as

$$\begin{aligned} z_l^{(R,B)}(k) &= \rho_l^{(R)}(k) - \rho_l^{(B)}(k) \\ &= \|\boldsymbol{r}_{r,R}(k) - \boldsymbol{r}_{leo,l}(k)\|_2 - \|\boldsymbol{r}_{r,B}(k) - \boldsymbol{r}_{leo,l}(k)\|_2 \\ &\quad + c\delta t_r^{(R,B)}(k) \\ &\quad + c\delta t_{trop,l}^{(R,B)}(k) + c\delta t_{iono,l}^{(R,B)}(k) + \nu_{\rho,l}^{(R,B)}(k), \end{aligned}$$

where

$$\begin{aligned} \delta t_r^{(R,B)}(k) &= \delta t_r^{(R)}(k) - \delta t_r^{(B)}(k) \\ \delta t_{trop,l}^{(R,B)}(k) &= \delta t_{trop,l}^{(R)}(k) - \delta t_{trop,l}^{(B)}(k) \\ \delta t_{iono,l}^{(R,B)}(k) &= \delta t_{iono,l}^{(R)}(k) - \delta t_{iono,l}^{(B)}(k) \\ \nu_{\rho,l}^{(R,B)}(k) &= \nu_{\rho,l}^{(R)}(k) - \nu_{\rho,l}^{(B)}(k). \end{aligned}$$

2) Doppler Measurement Model: The Doppler measurement f_D extracted by the LEO receiver is related to the pseudorange rate measurement $\dot{\rho}$ as

$$\dot{\rho} = -\frac{c}{f_c} f_D \quad (7)$$

where f_c is the LEO SV carrier frequency. The pseudorange rate measurement from the i-th receiver to the l-th LEO SV is modeled as

$$\begin{aligned} \dot{\rho}_l^{(i)}(k) &= [\dot{\boldsymbol{r}}_{r,i}(k) - \dot{\boldsymbol{r}}_{leo,l}(k)]^{\mathsf{T}} \frac{\boldsymbol{r}_{r,i}(k) - \boldsymbol{r}_{leo,l}(k)}{\|\boldsymbol{r}_{r,i}(k) - \boldsymbol{r}_{leo,l}(k)\|_2} \\ &\quad + c[\dot{\delta} t_{r,i}(k) - \dot{\delta} t_{leo,l}(k)] \\ &\quad + c\dot{\delta} t_{trop,l}^{(i)}(k) + c\dot{\delta} t_{iono,l}^{(i)}(k) + \nu_{\dot{\rho},l}^{(i)}(k) \end{aligned}$$

where $\dot{\boldsymbol{r}}_{r,i}$ and $\dot{\boldsymbol{r}}_{leo,l}$ are the 3-D velocity vectors of the i-th receiver and the l-th LEO SV in the ECEF reference frame; $\dot{\delta} t_{r,i}$ and $\dot{\delta} t_{leo,l}$ are the clock drifts of the i-th receiver and the l-th LEO SV, respectively; $\dot{\delta} t_{iono,l}^{(i)}$ and $\dot{\delta} t_{trop,l}^{(i)}$ are the ionospheric and tropospheric delay rates (drifts), respectively; and $\nu_{\dot{\rho},l}^{(i)}$ is the pseudorange rate measurement noise, which is modeled as a discrete-time zero-mean white Gaussian sequence with variance $\sigma_{\dot{\rho},l}^{(i)}(k)$.

The differential pseudorange rate measurement model across the rover and the base is defined as

$$\begin{aligned} z_l^{(R,B)}(k) &= \dot{\rho}_l^{(R)}(k) - \dot{\rho}_l^{(B)}(k) \\ &= [\dot{\boldsymbol{r}}_{r,R}(k) - \dot{\boldsymbol{r}}_{leo,l}(k)]^{\mathsf{T}} \frac{\boldsymbol{r}_{r,R}(k) - \boldsymbol{r}_{leo,l}(k)}{\|\boldsymbol{r}_{r,R}(k) - \boldsymbol{r}_{leo,l}(k)\|_2} \\ &\quad - [\dot{\boldsymbol{r}}_{r,B}(k) - \dot{\boldsymbol{r}}_{leo,l}(k)]^{\mathsf{T}} \frac{\boldsymbol{r}_{r,B}(k) - \boldsymbol{r}_{leo,l}(k)}{\|\boldsymbol{r}_{r,B}(k) - \boldsymbol{r}_{leo,l}(k)\|_2} \\ &\quad + c\dot{\delta} t_r^{(R,B)}(k) + c\dot{\delta} t_{trop,l}^{(R,B)}(k) + c\dot{\delta} t_{iono,l}^{(R,B)}(k) \\ &\quad + \nu_l^{(R,B)}(k), \end{aligned} \quad (8)$$

where

$$\begin{aligned} \dot{\delta} t_r^{(R,B)}(k) &= \dot{\delta} t_r^{(R)}(k) - \dot{\delta} t_r^{(B)}(k) \\ \dot{\delta} t_{trop,l}^{(R,B)}(k) &= \dot{\delta} t_{trop,l}^{(R)}(k) - \dot{\delta} t_{trop,l}^{(B)}(k) \\ \dot{\delta} t_{iono,l}^{(R,B)}(k) &= \dot{\delta} t_{iono,l}^{(R)}(k) - \dot{\delta} t_{iono,l}^{(B)}(k) \\ \nu_{\dot{\rho},l}^{(R,B)}(k) &= \nu_{\dot{\rho},l}^{(R)}(k) - \nu_{\dot{\rho},l}^{(B)}(k). \end{aligned}$$

The differential measurements eliminate the time-varying LEO SV clock biases and drifts; however, the relative clock bias and drift between the rover and the base cannot be resolved. Thus, this clock difference will be dynamically estimated in the EKF that is described in what follows.

E. EKF Formulation

In this framework, a stationary base with known position states and a mobile rover equipped with an IMU are considered. Thus, an EKF is formulated to estimate the rover's states, the clock state difference, and the LEO SV's position and velocity states. The EKF state vector is given by

$$\begin{aligned} \boldsymbol{x} &= [\boldsymbol{x}_r,\, \boldsymbol{x}_{clk},\, \boldsymbol{x}_{leo,1},\, ...,\, \boldsymbol{x}_{leo,L}]^\mathsf{T} \\ \boldsymbol{x}_r &= [{}^b_g\bar{\boldsymbol{q}}^\mathsf{T},\, \boldsymbol{r}_r^\mathsf{T},\, \dot{\boldsymbol{r}}_r^\mathsf{T},\, \boldsymbol{b}_{gyr}^\mathsf{T},\, \boldsymbol{b}_{acc}^\mathsf{T}]^\mathsf{T} \\ \boldsymbol{x}_{leo,l} &= [\boldsymbol{r}_{leo,l}^\mathsf{T},\, \dot{\boldsymbol{r}}_{leo,l}^\mathsf{T}]^\mathsf{T} \end{aligned}$$

where $\boldsymbol{x}_r$ is the vehicle's state vector, composed of ${}^b_g\bar{\boldsymbol{q}}$, which is a four-dimensional unit quaternion representing the orientation of the body frame $\{b\}$ fixed at the IMU with respect to the global frame $\{g\}$; $\boldsymbol{r}_r$ and $\dot{\boldsymbol{r}}_r$ are the 3-D position and velocity of the vehicle expressed in $\{g\}$; and $\boldsymbol{b}_{gyr}$ and $\boldsymbol{b}_{acc}$ are the 3-D biases of the IMU's gyroscope and accelerometer, respectively, expressed in $\{\mathrm{b}\}$. The vector $\boldsymbol{x}_{clk}$ is the clock state, composed of the difference between the rover and the bases' clock states, The vector $\boldsymbol{x}_{leo,l}$ is the state vector of the l-th LEO SV, composed of the SV's position $\boldsymbol{r}_{leo,l}$ and velocity $\dot{\boldsymbol{r}}_{leo,l}$ vectors, expressed in the ECEF frame.

The EKF predicts the vehicle's orientation, position, and velocity using the IMU angular velocity and acceleration measurements processed through the strap-down INS kinematic equations [53]. The LEO SV's position and velocity states are propagated through the two-body with J_2 model in the ECI frame, described in Section II-B. The EKF update is performed using the GNSS measurements when available, altimeter readings, and LEO pseudorange or Doppler measurements, and finally outputs a state estimate and a corresponding estimation error covariance matrix.

III. Simulation Results

This section presents the simulation results via a high-fidelity simulator to assess the performance of the proposed differential STAN framework.

A. Simulation Overview

The simulation considered a fixed-wing aerial vehicle that traveled a 28 km trajectory for 300 seconds over Columbus, Ohio, USA. The vehicle was equipped with a tactical-grade IMU, an altimeter, a GNSS receiver, and a Starlink LEO receiver that produced pseudorange and Doppler measurements. The simulated environment also included three base stations, equipped with Starlink LEO receivers that produced pseudorange and Doppler observables which were communicated to the aerial vehicle along with the base position positions. The minimum, mean, and maximum baseline distance between the aerial vehicle along its simulated trajectory and the 3 base stations are summarized in Table I.

TABLE I
MINIMUM, MEAN, AND MAXIMUM BASELINE DISTANCE BETWEEN THE AERIAL VEHICLE AND THE THREE BASE STATIONS IN THE SIMULATION.

	Min (km)	**Mean** (km)	**Max** (km)
Base 1	2.81	5.37	8.16
Base 2	1.89	6.01	9.97
Base 3	1.56	4.84	11.2

GNSS signals were made available to the aerial vehicle for the first 60 seconds of flight time, during which the GNSS measurements are fused with the INS in a loosely coupled fashion, while the LEO observables were used to refine the estimates of the LEO SVs ephemerides and the rover-base(s) clock differences. During the last 240 seconds, the GNSS signals were made unavailable to the vehicle which operated in STAN mode: the altimeter measurements and LEO observables aided the on-board INS, while simultaneously estimating the LEO SVs' ephemerides and clock differences.

The IMU measurements were generated from the vehicle's kinematics with the gyroscope and accelerometer bias instability and noise density parameters summarized in Table II. The clock bias and drift of the aerial vehicle, base stations, and LEO SVs were simulated according to (4). The aerial vehicle and the base stations were equipped with high-quality OCXOs, while the LEO SVs CSACs. The process noise of these clocks was determined according to the power-law coefficients listed in Table II.

TABLE II
SIMULATION SETTINGS

IMU Parameters	
Gyroscope Bias Instability	1.5° / hr
Gyroscope Noise Density	1.5° / hr / $\sqrt{\text{Hz}}$
Accelerometer Bias Instability	100 μg
Accelerometer Noise Density	110 $\mu\text{g}/\sqrt{\text{Hz}}$
Oscillator Power Law Coefficients	
High-quality OCXO $\{h_0, h_{-2}\}$	$\{2.6\times10^{-22}, 4.0\times10^{-26}\}$
CSAC $\{h_0, h_{-2}\}$	$\{7.2\times10^{-21}, 2.7\times10^{-27}\}$
Altimeter	
Measurement noise variance	1 m^2

The LEO SVs' trajectories were generated via Analytical Graphics Inc. (AGI) Systems Tool Kit (STK) using a High-Precision Orbit Propagator (HPOP) [54]. Fourteen Starlink LEO SVs were tracked and found to be visible with a minimum elevation of 15 degrees from Columbus on January 9, 2023, at 17:00 UTC. The orbits of these SVs are shown in Fig. 3.

Pseudorange and Doppler measurements were generated from the aerial vehicle and the three base stations to all visible LEO SVs according to (7) and (8), respectively. The measurement noise variances were calculated based on the predicted C/N_0 which was found from the log distance path

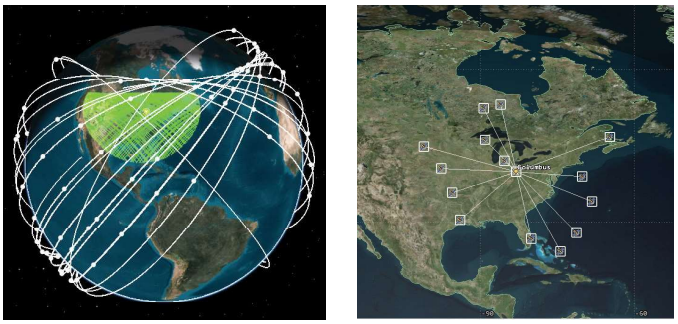

Fig. 3. Orbits of the simulated Starlink SVs with an access region above Columbus, Ohio, USA.

loss model

$$(C/N_0)_l(k) = P_0 - 10 \cdot \log_{10}(d_l(k)/D_0), \tag{9}$$

where P_0 = 56 dB-Hz is the nominal C/N_0 at a distance D_0=1,000 km and $d_l(k) = \|\boldsymbol{r}_{r,i}(k) - \boldsymbol{r}_{leo,l}(k)\|$ is the distance between the i-th receiver and the l-th LEO SV. Note that the measurement noise variances at the base(s) are communicated along with the measurements to the rover.

To demonstrate the benefit of aiding the INS using differential LEO measurements, two cases were considered:

- Standalone STAN: the aerial vehicle relied solely on the LEO observables that were extracted from its LEO receiver.
- Differential STAN: the aerial vehicle differenced its LEO measurements from those that are communicated from one, two, or three base stations as described in (7) and (8).

Both configurations were simulated using pseudorange or Doppler observables from the LEO receivers. Table III summarizes the achieved results.

TABLE III
SUMMARY OF SIMULATION RESULTS

	GNSS-INS	STAN	Differential STAN		
			1 Base	2 Bases	3 Bases
Pseudorange					
RMSE (m)	528	8.16	0.87	0.42	0.28
Final Error (m)	1,795	6.37	0.60	0.07	0.15
Doppler					
RMSE (m)	528	15.63	5.26	3.88	1.94
Final Error (m)	1,795	25.79	9.54	2.05	1.90

Fig. 4 illustrates the simulation environment showing the base station locations and the aerial vehicle's true and estimated trajectories via the GNSS-aided INS, STAN-aided INS, and differential STAN-aided INS. Fig. 5 shows the EKF estimation errors for pseudrange measurements with one base station, while Fig. 6 and Fig. 7 show the EKF uncertainties for pseudorange measurements with one, two, and three bases of the aerial vehicle's position states and one of the LEO SV's position states. Fig. 8 shows the EKF estimation errors for Doppler measurements with one base station, while Fig. 9 show the EKF uncertainties for Doppler measurements with one, two, and three bases of the aerial vehicle's position states and one of the LEO SV's position states.

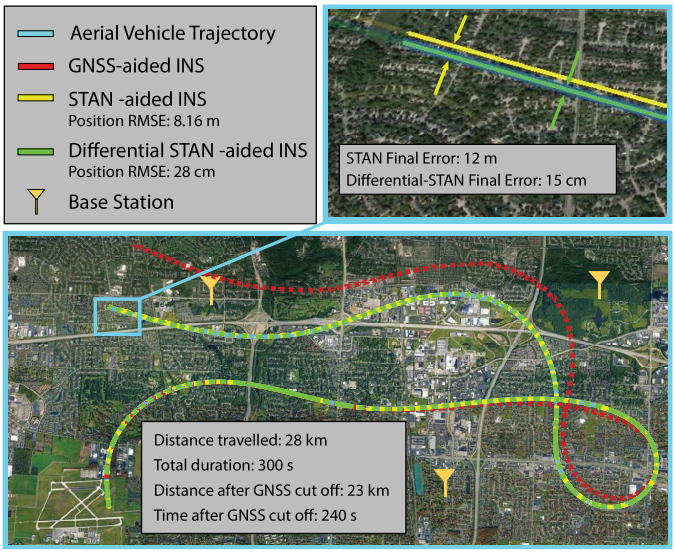

Fig. 4. Simulation results showing the aerial vehicle's trajectory and estimated trajectory with GNSS-aided INS, STAN, and Differential STAN with three base stations. Map data: Google Earth.

B. Discussion

Fig. 5 shows the quick divergence of the GNSS-INS errors upon GNSS cutoff. In contrast, the STAN errors diverge slowly in the East and North directions. The STAN velocity errors in the East and North directions appear to diverge slower than their corresponding position states. The error bounds diverge slower when pseudorange measurements are used compared to Doppler. The EKF errors of the differential STAN, where the vehicle is aided with LEO pseudorange observables from only one base, appear to converge during the simulation duration. Note that the altimeter measurements prevent the Up direction EKF errors from diverging in all configurations, with the STAN and differential STAN uncertainty bounds being smaller than those of the GNSS-INS.

Fig. 6 shows that the bounds are significantly tighter with the addition of the first base measurements, significantly tighten with the second base, but tighten slightly with the third. These results illustrate the benefit of incorporating LEO measurements from a single base station on the navigation solution, resulting in an RMSE decrease from 8.16 m to 87 cm in the pseudorange case, and from 15.63 m to 5.26 m in the Doppler case. Moreover, the RMSE decreases to 42 cm and 28 cm after the addition of the second and third base stations with pseudorange measurements, respectively, and to 2.05 m and 1.9 m with Doppler measurements, respectively. These results demonstrate the potential of accurate navigation using a relatively low number of LEO SVs in comparison with a standalone STAN framework [39].

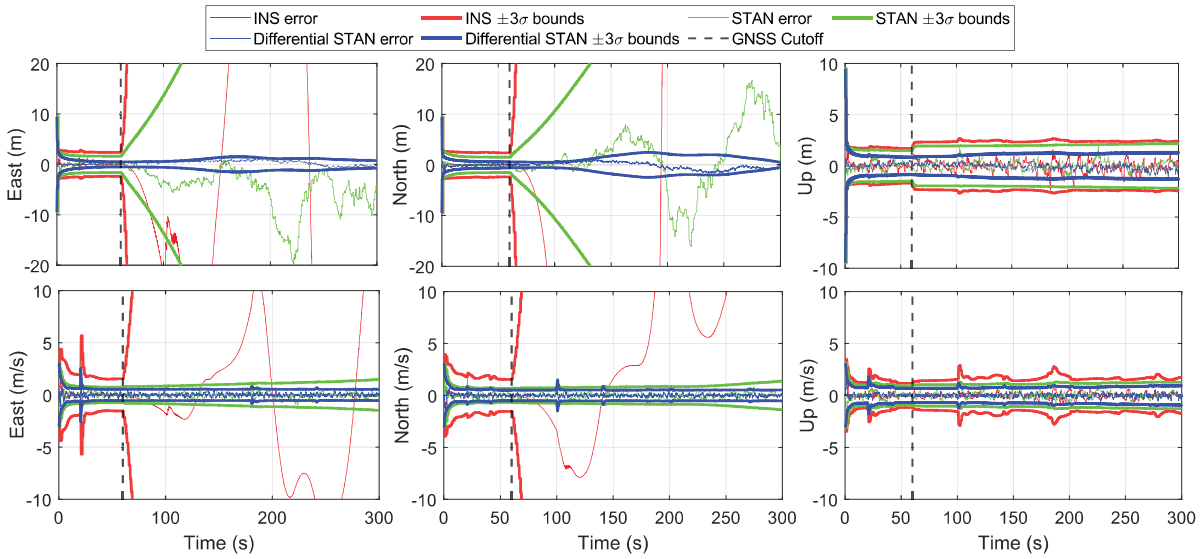

Fig. 5. EKF estimation error plots and $\pm 3\sigma$ bounds of the aerial vehicle states for GNSS-INS, STAN, and one base differential STAN LEO pseudorange-aided INS. The first and second rows correspond to the position and velocity states, respectively, of the vehicle in the ENU frame.

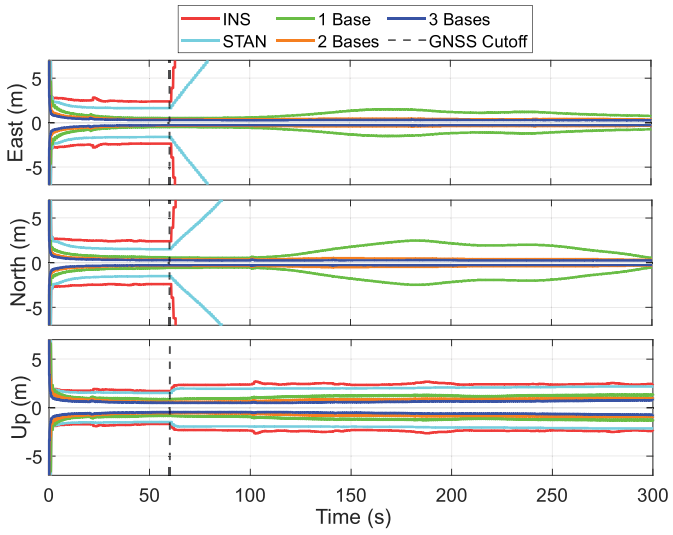

Fig. 6. EKF $\pm 3\sigma$ estimation error bounds of the aerial vehicle states in the ENU frame with pseudorange-aided INS for varying number of base stations.

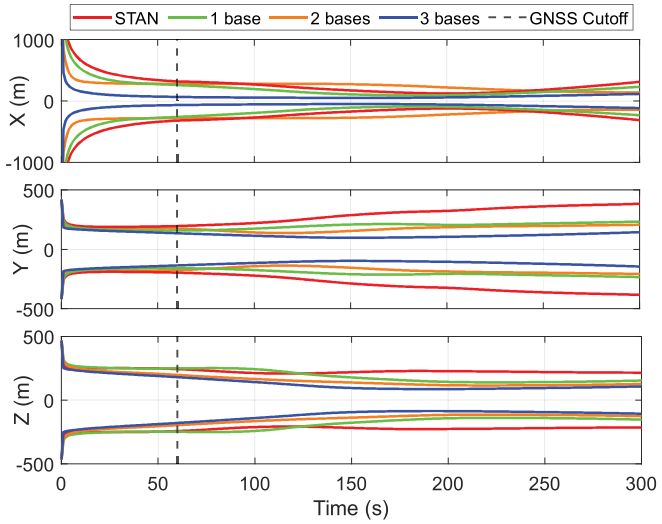

Fig. 7. EKF $\pm 3\sigma$ estimation error bounds of the Starlink-1154 LEO SV position states in the ECEF frame, tracked with pseudorange measurements for varying number of base stations.

This significant improvement presented by the differential framework can be attributed to (i) elimination of the dynamic LEO SV clocks from the estimation state vector, (ii) additional information communicated from the measurements of the base stations that have known positions, (iii) and the compensation of ephemeris error in the differenced measurements. Note that while the differential framework introduces the estimation of the dynamic clock difference between the rover and bases, this issue is outweighed by the aforementioned advantages.

Fig. 7 shows that the LEO SV tracking error bounds are tighter with the addition of the first base measurements, and the uncertainty gradually tighten with additional base stations. Similar results were observed for other LEO SVs.

Fig. 8 and Fig. 9 reveal that the performance with Doppler measurements is slightly worse than that achieved with pseudorange measurements.

IV. Experimental Results

This section validates the differential STAN framework discussed in Section II by showing experimental results of a UAV navigating with carrier phase measurements from 2 Orbcomm LEO SVs. The experimental setup, depicted in Fig. 10, was the same as the one discussed in [45], where a DJI Matrice 600 UAV traveled a total of 2.28 km in 120 seconds over Irvine, California, USA. Over the course of

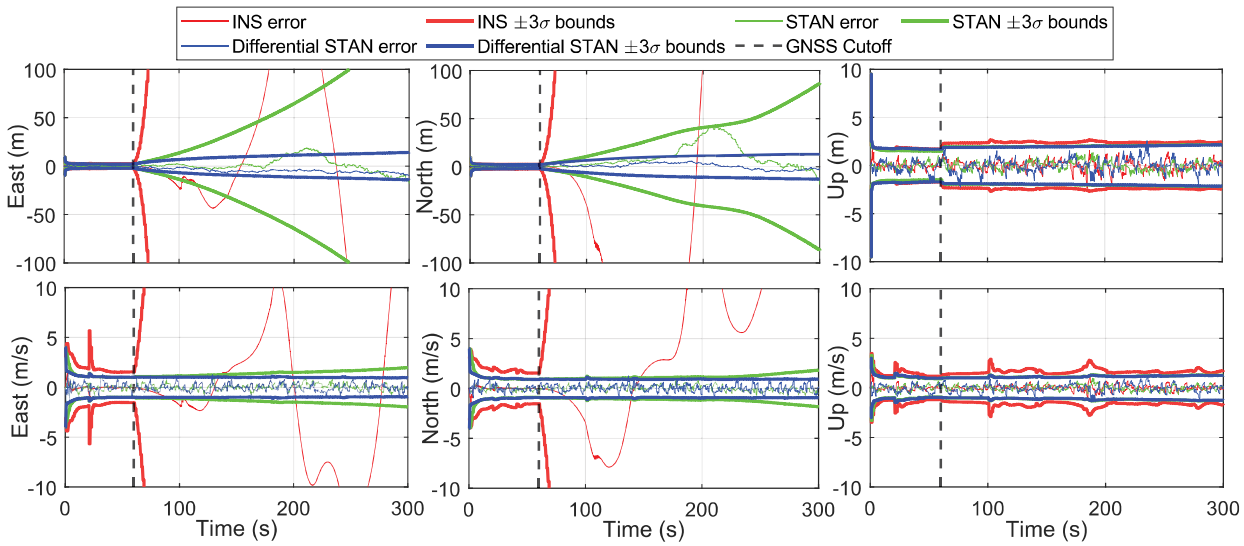

Fig. 8. EKF estimation error plots and $\pm 3\sigma$ bounds of the aerial vehicle states GNSS-INS, STAN, and one base differential STAN LEO Doppler-aided INS. The first and second rows correspond to the position and velocity states, respectively, of the vehicle in the ENU frame.

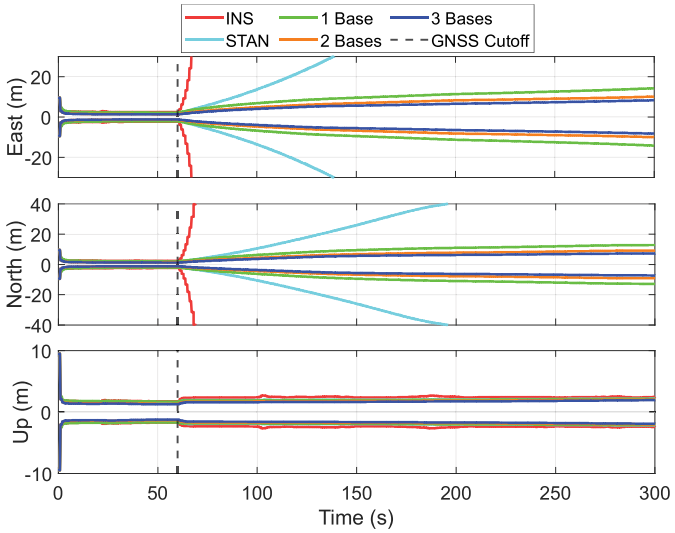

Fig. 9. EKF $\pm 3\sigma$ estimation error bounds of the aerial vehicle states in the ENU frame with Doppler-aided INS for varying number of base stations.

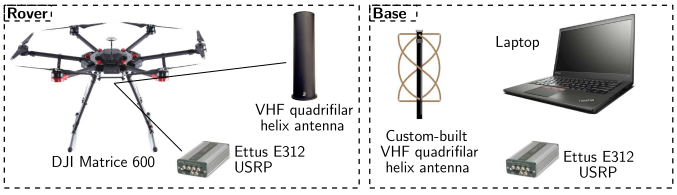

Fig. 10. Experimental hardware used at the base and rover

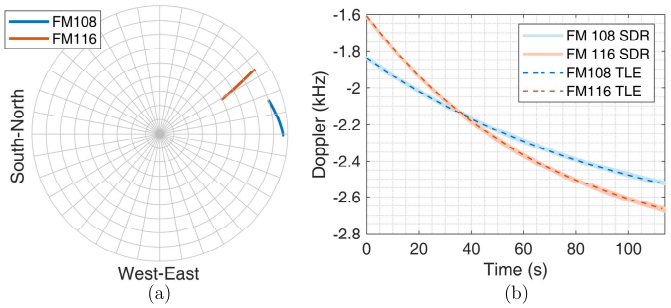

Fig. 11. (a) Sky plot of the 2 Orbcomm SVs during the experiment. (b) The measured Doppler frequencies using the rover's SDR and the expected Doppler calculated from the TLE for both Orbcomm SVs.

the experiment, the receivers on the UAV and base station were listening to the same 2 Orbcomm SVs, namely FM 108 and FM 116 (see Fig. 11). The 2 receivers were within a range of 1 km over the whole duration; hence, ionospheric and tropospheric delays were negligible. Since no raw IMU data were available from the UAV, a velocity random walk dynamics was assumed for the UAV. The EKF formulation is discussed in [45].

To demonstrate the benefit of navigating with differential STAN, the UAV's 3-D position and velocity were estimated and compared to: (i) non-differential STAN framework employing the same carrier phase measurements from the UAV's receiver only and (ii) non-STAN differential framework using LEO SV positions estimated from TLE files. The initial UAV'S position and velocity were obtained from the UAV's GNSS/INS, whereas a prior for the SVs' states was obtained from TLE at the time of the experiment. These priors were used to initialize the EKF, which used single difference LEO measurements to simultaneously estimate the states of the UAV and SVs.

Fig. 13 shows the EKF position estimation errors with the $\pm 3\sigma$ bounds. Note that as the UAV traveled mainly in the North direction, the bounds in the East direction diverges at a higher rate, making it poorly estimable, while the altimeter maintains accurate vertical positioning. Table IV summarizes

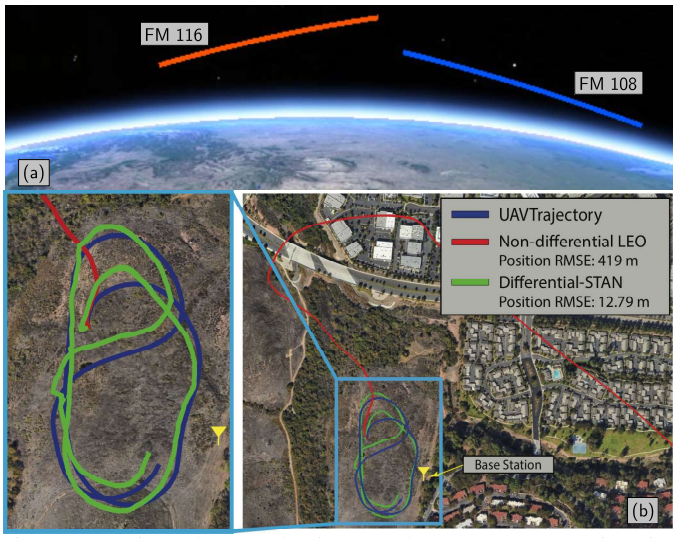

Fig. 12. Experimental results showing (a) Orbcomm LEO SVs' trajectories and (b) UAV's trajectory and estimated trajectory with non-differential TLE-tracked LEO and differential STAN, with carrier-phase LEO measurements. Map data: Google Earth.

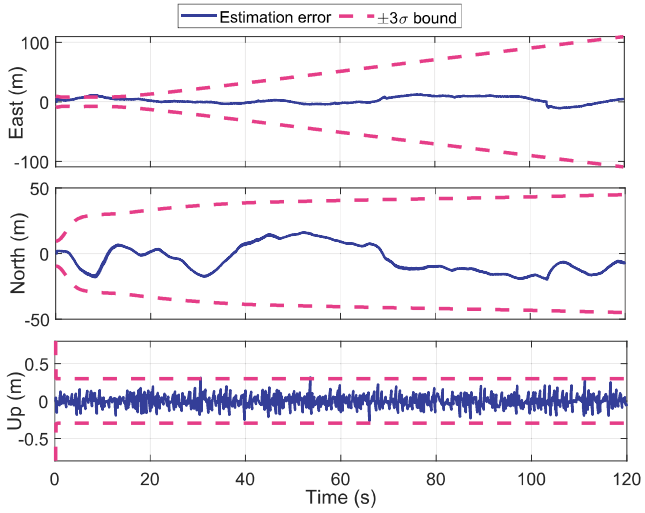

Fig. 13. EKF estimation error plots and $\pm 3\sigma$ bounds of the aerial vehicle position states in the ENU frame, with LEO carrier-phase differential STAN.

the results for the 3 different frameworks and Fig. 12 shows the LEO SV trajectories and UAV's true and estimated trajectories. Table IV summarizes the navigation results. Note that the differential STAN frameworks yielded acceptable navigation performance, while the TLE-based differential framework being slightly less accurate. It is worth highlighting that the achieved results are noteworthy, considering that no IMU was used and signals from only two LEO SVs were exploited. It is expected that the navigation performance would improve dramatically if more LEO SVs are used.

V. Conclusion

This paper revealed the tremendous potential of differential STAN to achieve submeter-accurate navigation, despite the poorly known LEO SV ephemerides (errors on the order of several kilometers). A simulation study was conducted

TABLE IV
Experimental results: 3-D position RMSEs.

Framework	SV position source	RMSE (m)
Differential	STAN	12.79
Differential	TLE	13.0
Non-differential	TLE	419

to evaluate the performance of the proposed framework with pseudorange and Doppler measurements from 14 Starlink LEO SVs. The results were compared to standalone STAN, showing a 3-D RMSE reduction from 8.16 m to 28 cm with 3 base stations using pseudorange measurements and 1.94 m with Doppler measurements. A UAV experimental demonstration using carrier phase observables from 2 Orbcomm LEO SVs was shown to reduce the position RMSE from 419 m in the non-differential case to 12.79 m with the proposed differential framework.

Acknowledgment

The authors would like to thank to thank Dr. Chris Bartone for the insightful discussions and Joe Khalife, Joshua Morales, and Sharbel Kozhaya for their help in experimental data collection and processing.

References

[1] Z. Kassas, P. Closas, and J. Gross, "Navigation systems for autonomous and semi-autonomous vehicles: Current trends and future challenges," *IEEE Aerospace and Electronic Systems Magazine*, vol. 34, pp. 82–84, May 2019.

[2] M. Braasch, "Inertial navigation systems," in *Aerospace Navigation Systems*, John Wiley & Sons, Ltd, 2016.

[3] G. McGraw and M. Braasch, "GNSS multipath mitigation using gated and high resolution correlator concepts," in *Proceedings of ION National Technical Meeting*, pp. 333–342, January 1999.

[4] Z. Kassas, "Position, navigation, and timing technologies in the 21st century," vol. 1, ch. 22: Robust Positioning in the Presence of Multipath and NLOS GNSS Signals, pp. 551–589, Wiley-IEEE, 2021.

[5] C. Hegarty, D. Bobyn, J. Grabowski, and A. Van Dierendonck, "An overview of the effects of out-of-band interference on GNSS receivers," *NAVIGATION, Journal of the Institute of Navigation*, vol. 67, pp. 143–161, March 2020.

[6] R. Ioannides, T. Pany, and G. Gibbons, "Known vulnerabilities of global navigation satellite systems, status, and potential mitigation techniques," *Proceedings of the IEEE*, vol. 104, pp. 1174–1194, February 2016.

[7] D. Miralles, A. Bornot, P. Rouquette, N. Levigne, D. Akos, Y.-H.Chen, S. Lo, and T. Walter, "An assessment of GPS spoofing detection via radio power and signal quality monitoring for aviation safety operations," *IEEE Intelligent Transportation Systems Magazine*, vol. 12, pp. 136–146, June 2020.

[8] J. Raquet *et al.*, "Position, navigation, and timing technologies in the 21st century," vol. 2, Part D: Position, Navigation, and Timing Using Radio Signals-of-Opportunity, ch. 35–43, pp. 1115–1412, Wiley-IEEE, 2021.

[9] X. Chen, Q. Wei, F. Wang, Z. Jun, S. Wu, and A. Men, "Super-resolution time of arrival estimation for a symbiotic FM radio data system," *IEEE Transactions on Broadcasting*, vol. 66, pp. 847–856, December 2020.

[10] M. Psiaki and B. Slosman, "Tracking digital FM OFDM signals for the determination of navigation observables," *NAVIGATION, Journal of the Institute of Navigation*, vol. 69, no. 2, 2022.

[11] J. Khalife and Z. Kassas, "Opportunistic UAV navigation with carrier phase measurements from asynchronous cellular signals," *IEEE Transactions on Aerospace and Electronic Systems*, vol. 56, pp. 3285–3301, August 2020.

[12] L. Chen, X. Zhou, F. Chen, L. Yang, and R. Chen, "Carrier phase ranging for indoor positioning with 5G NR signals," *IEEE Internet of Things Journal*, vol. 9, pp. 10908–10919, July 2022.

[13] T. Hong, J. Sun, T. Jin, Y. Yi, and J. Qu, "Hybrid positioning with DTMB and LTE signals," in *Proceedings of International Wireless Communications and Mobile Computing*, pp. 303–307, July 2021.

[14] Z. Jiao, L. Chen, X. Lu, Z. Liu, X. Zhou, Y. Zhuang, and G. Guo, "Carrier phase ranging with DTMB signals for urban pedestrian localization and GNSS aiding," *Remote Sensing*, vol. 15, no. 2, pp. 423–446, 2023.

[15] M. Leng, F. Quitin, W. Tay, C. Cheng, S. Razul, and C. See, "Anchor-aided joint localization and synchronization using SOOP: Theory and experiments," *IEEE Transactions on Wireless Communications*, vol. 15, pp. 7670–7685, November 2016.

[16] Z. Tan, H. Qin, L. Cong, and C. Zhao, "New method for positioning using IRIDIUM satellite signals of opportunity," *IEEE Access*, vol. 7, pp. 83412–83423, 2019.

[17] Z. Kassas, M. Neinavaie, J. Khalife, N. Khairallah, J. Haidar-Ahmad, S. Kozhaya, and Z. Shadram, "Enter LEO on the GNSS stage: Navigation with Starlink satellites," *Inside GNSS Magazine*, vol. 16, no. 6, pp. 42–51, 2021.

[18] N. Jardak and Q. Jault, "The potential of LEO satellite-based opportunistic navigation for high dynamic applications," *Sensors*, vol. 22, no. 7, pp. 2541–2565, 2022.

[19] M. Hartnett, "Performance assessment of navigation using carrier Doppler measurements from multiple LEO constellations," Master's thesis, Air Force Institute of Technology, Ohio, USA, 2022.

[20] N. Jardak and R. Adam, "Practical use of Starlink downlink tones for positioning," *Sensors*, vol. 23, pp. 3234–3253, March 2023.

[21] Y. Gao, X. Zhao, S. Wang, Y. Xiang, C. Huang, and Y. Hua, "Positioning via GEO communication satellites' signals of opportunity," *IET Radar, Sonar Navigation*, vol. 15, pp. 1472–1482, July 2021.

[22] R. Whiton, J. Chen, T. Johansson, and F. Tufvesson, "Urban navigation with LTE using a large antenna array and machine learning," in *Proceedings of IEEE Vehicular Technology Conference*, pp. 1–5, 2022.

[23] J. Khalife and Z. Kassas, "On the achievability of submeter-accurate UAV navigation with cellular signals exploiting loose network synchronization," *IEEE Transactions on Aerospace and Electronic Systems*, vol. 58, pp. 4261–4278, October 2022.

[24] S. Bilardi, "A GNSS signal simulator and processor for evaluating acquisition and tracking of GPS-like signals from satellites in LEO," Master's thesis, University of Colorado at Boulder, CO, USA, 2021.

[25] J. Khalife, M. Neinavaie, and Z. Kassas, "The first carrier phase tracking and positioning results with Starlink LEO satellite signals," *IEEE Transactions on Aerospace and Electronic Systems*, vol. 56, pp. 1487–1491, April 2022.

[26] C. Huang, H. Qin, C. Zhao, and H. Liang, "Phase - time method: Accurate Doppler measurement for Iridium NEXT signals," *IEEE Transactions on Aerospace and Electronic Systems*, vol. 58, no. 6, pp. 5954–5962, 2022.

[27] C. Zhao, H. Qin, and Z. Li, "Doppler measurements from multiconstellations in opportunistic navigation," *IEEE Transactions on Instrumentation and Measurement*, vol. 71, pp. 1–9, 2022.

[28] U. Singh, M. Shankar, and B. Ottersten, "Opportunistic localization using LEO signals," in *Proceedings of Asilomar Conference on Signals, Systems, and Computers*, pp. 894–899, 2022.

[29] H. More, E. Cianca, and M. Sanctis, "Positioning performance of LEO mega constellations in deep urban canyon environments," in *Proceedings of International Symposium on Wireless Personal Multimedia Communications*, pp. 256–260, 2022.

[30] Z. Kassas, J. Morales, and J. Khalife, "New-age satellite-based navigation – STAN: simultaneous tracking and navigation with LEO satellite signals," *Inside GNSS Magazine*, vol. 14, no. 4, pp. 56–65, 2019.

[31] F. Farhangian, H. Benzerrouk, and R. Landry, "Opportunistic in-flight INS alignment using LEO satellites and a rotatory IMU platform," *Aerospace*, vol. 8, no. 10, pp. 280–281, 2021.

[32] F. Prol, R. Ferre, Z. Saleem, P. Välisuo, C. Pinell, E. Lohan, M. Elsanhoury, M. Elmusrati, S. Islam, K. Celikbilek, K. Selvan, J. Yliaho, K. Rutledge, A. Ojala, L. Ferranti, J. Praks, M. Bhuiyan, S. Kaasalainen, and H. Kuusniemi, "Position, navigation, and timing (PNT) through low earth orbit (LEO) satellites: A survey on current status, challenges, and opportunities," *IEEE Access*, vol. 10, pp. 83971–84002, 2022.

[33] M. Neinavaie, J. Khalife, and Z. Kassas, "Cognitive opportunistic navigation in private networks with 5G signals and beyond," *IEEE Journal of Selected Topics in Signal Processing*, vol. 16, no. 1, pp. 129–143, 2022.

[34] S. Kozhaya and Z. Kassas, "Blind receiver for LEO beacon estimation with application to UAV carrier phase differential navigation," in *Proceedings of ION GNSS Conference*, pp. 2385–2397, 2022.

[35] M. Neinavaie, J. Khalife, and Z. Kassas, "Acquisition, Doppler tracking, and positioning with Starlink LEO satellites: First results," *IEEE Transactions on Aerospace and Electronic Systems*, vol. 58, pp. 2606–2610, June 2022.

[36] S. Kozhaya, H. Kanj, and Z. Kassas, "Multi-constellation blind beacon estimation, Doppler tracking, and opportunistic positioning with OneWeb, Starlink, Iridium NEXT, and Orbcomm LEO satellites," in *Proceedings of IEEE/ION Position, Location, and Navigation Symposium*, April 2023. accepted.

[37] North American Aerospace Defense Command (NORAD), "Two-line element sets." http://celestrak.com/NORAD/elements/.

[38] D. Vallado and P. Crawford, "SGP4 orbit determination," in *Proceedings of AIAA/AAS Astrodynamics Specialist Conference and Exhibit*, pp. 6770–6799, August 2008.

[39] Z. Kassas, N. Khairallah, and S. Kozhaya, "Ad astra: Simultaneous tracking and navigation with megaconstellation LEO satellites," *IEEE Aerospace and Electronic Systems Magazine*, 2023. accepted.

[40] N. Khairallah and Z. Kassas, "An interacting multiple model estimator of LEO satellite clocks for improved positioning," in *Proceedings of IEEE Vehicular Technology Conference*, pp. 1–5, 2022.

[41] K. Wang and A. El-Mowafy, "LEO satellite clock analysis and prediction for positioning applications," *Geo-spatial Information Science*, vol. 25, no. 1, pp. 14–33, 2022.

[42] B. Parkinson and P. Enge, "Differential GPS," *Global Positioning System: Theory and applications.*, vol. 2, pp. 3–50, 1996.

[43] P. Hwang, G. McGraw, and J. Bader, "Enhanced differential GPS carrier-smoothed code processing using dual-frequency measurements," *NAVIGATION, Journal of the Institute of Navigation*, vol. 46, no. 2, pp. 127–138, 1999.

[44] K. Pesyna, Z. Kassas, R. Heath, and T. Humphreys, "A phase-reconstruction technique for low-power centimeter-accurate mobile positioning," *IEEE Transactions on Signal Processing*, vol. 62, pp. 2595–2610, May 2014.

[45] J. Khalife and Z. Kassas, "Performance-driven design of carrier phase differential navigation frameworks with megaconstellation LEO satellites," *IEEE Transactions on Aerospace and Electronic Systems*, pp. 1–20, 2023. accepted.

[46] M. Neinavaie, Z. Shadram, S. Kozhaya, and Z. M. Kassas, "First results of differential Doppler positioning with unknown Starlink satellite signals," in *Proceedings of IEEE Aerospace Conference*, pp. 1–14, March 2022.

[47] C. Zhao, H. Qin, N. Wu, and D. Wang, "Analysis of baseline impact on differential doppler positioning and performance improvement method for LEO opportunistic navigation," *IEEE Transactions on Instrumentation and Measurement*, pp. 1–10, 2023.

[48] J. Morales, J. Khalife, U. Santa Cruz, and Z. Kassas, "Orbit modeling for simultaneous tracking and navigation using LEO satellite signals," in *Proceedings of ION GNSS Conference*, pp. 2090–2099, September 2019.

[49] N. Khairallah and Z. Kassas, "Ephemeris closed-loop tracking of LEO satellites with pseudorange and Doppler measurements," in *Proceedings of ION GNSS Conference*, pp. 2544–2555, September 2021.

[50] B. Tapley, M. Watkins, C. Ries, W. Davis, R. Eanes, S. Poole, H. Rim, B. Schutz, C. Shum, R. Nerem, F. Lerch, J. Marshall, S. Klosko, N. Pavlis, and R. Williamson, "The Joint Gravity Model 3," *Journal of Geophysical Research*, vol. 101, pp. 28029–28049, December 1996.

[51] R. Brown and P. Hwang, *Introduction to Random Signals and Applied Kalman Filtering with Matlab Exercises*. John Wiley & Sons, fourth ed., 2012.

[52] A. Thompson, J. Moran, and G. Swenson, *Interferometry and Synthesis in Radio Astronomy*. John Wiley & Sons, second ed., 2001.

[53] P. Groves, *Principles of GNSS, Inertial, and Multisensor Integrated Navigation Systems*. Artech House, second ed., 2013.

[54] Systems Tool Kit (STK), "High-Precision Orbit Propagator (HPOP)." https://help.agi.com/stk/11.0.1/Content/hpop/hpop.htm, September 2016.